Biophysical Journal
Article

Biophysical Society

The Poisson Ratio of the Cellular Actin Cortex Is Frequency Dependent

Marcel Mokbel,[1] Kamran Hosseini,[2,3] Sebastian Aland,[1,*] and Elisabeth Fischer-Friedrich[2,3,*]
[1]Faculty of Informatics/Mathematics, Hochschule für Technik und Wirtschaft, Dresden, Germany; [2]Cluster of Excellence Physics of Life and [3]Biotechnology Center, Technische Universität Dresden, Dresden, Germany

ABSTRACT Cell shape changes are vital for many physiological processes such as cell proliferation, cell migration, and morphogenesis. They emerge from an orchestrated interplay of active cellular force generation and passive cellular force response, both crucially influenced by the actin cytoskeleton. To model cellular force response and deformation, cell mechanical models commonly describe the actin cytoskeleton as a contractile isotropic incompressible material. However, in particular at slow frequencies, there is no compelling reason to assume incompressibility because the water content of the cytoskeleton may change. Here, we challenge the assumption of incompressibility by comparing computer simulations of an isotropic actin cortex with tunable Poisson ratio to measured cellular force response. Comparing simulation results and experimental data, we determine the Poisson ratio of the cortex in a frequency-dependent manner. We find that the Poisson ratio of the cortex decreases in the measured frequency regime analogous to trends reported for the Poisson ratio of glassy materials. Our results therefore indicate that actin cortex compression or dilation is possible in response to acting forces at sufficiently fast timescales. This finding has important implications for the parameterization in active gel theories that describe actin cytoskeletal dynamics.

SIGNIFICANCE Cell shape changes are vital for many physiological processes such as cell migration and morphogenesis. They emerge from an interplay of active cellular force generation and cell mechanical properties, both crucially influenced by the actin cytoskeleton. Cell mechanical models commonly make the simplifying assumption that the actin cytoskeleton is an incompressible material with the Poisson ratio 0.5. Here, we present a new technique for the measurement of the actin cytoskeletal Poisson ratio. Comparing results from computer simulations and experimental data, we determine the Poisson ratio of the actin cytoskeleton, taking into account the timescale-dependent nature of its mechanics. Our findings refute the prevalent assumption that the cytoskeleton can in general be modeled as an incompressible material with the Poisson ratio 0.5.

INTRODUCTION

The actin cytoskeleton, a cross-linked meshwork of actin polymers, is a key structural element that crucially influences mechanical properties of cells (1). In fact, for rounded mitotic cells, the mitotic actin cortex—a thin actin cytoskeleton layer attached to the plasma membrane—could be shown to be the dominant mechanical structure in whole-cell deformations (2). In the past, cell mechanical models have been developed to rationalize cell deformation in different biological systems (3,4). Such models require being parameterized by cell mechanical parameters. The mechanics of a simple isotropic elastic material is fully characterized by two mechanical parameters, e.g., its shear modulus G and its Poisson ratio ν. The Poisson ratio rates the magnitude of the Poisson effect, which is the expansion of the material in directions perpendicular to the direction of a compression; $\nu = 0.5$ corresponds to an infinite bulk modulus of the material and thus incompressibility.

Commonly, cell mechanical models describe the actin cytoskeleton as a contractile isotropic incompressible material (5). Incompressibility of the actin cytoskeleton is motivated by the incompressibility of water and the high water content in the actin cytoskeleton (6). This assumption is justified for high-frequency deformations because in this case, substantial water movement past the elastic scaffold of the polymerized actin meshwork would give rise to strong friction and is thus energetically suppressed (see Supporting Materials and Methods, Section 1). The anticipated high-frequency incompressibility

Submitted December 11, 2019, and accepted for publication March 2, 2020.
*Correspondence: sebastian.aland@htw-dresden.de or elisabeth.fischer-friedrich@tu-dresden.de
Editor: Ana-Suncana Smith.
https://doi.org/10.1016/j.bpj.2020.03.002
© 2020 Biophysical Society.

was confirmed experimentally in in vitro reconstituted actin meshworks in a frequency range of 500–10,000 Hz (7). However, in particular at slow frequencies, there is no compelling reason to assume incompressibility because the water content of the cytoskeleton may change via water fluxes past the cytoskeletal scaffold, leading to a bulk compression or dilation. Furthermore, the actin cytoskeleton is subject to dynamic turnover (1) and exhibits viscoelastic material properties (2–4,8). Therefore, it is expected that the cortical Poisson ratio is frequency dependent, as has been reported for other viscoelastic materials such as acrylic glass. There, the Poisson ratio was shown to increase from 0.32 to 0.5 for increasing timescales (9,10).

Here, we critically examine the assumption of actin cortex incompressibility by measuring the Poisson ratio of the actin cortex independent of the frequency of time-periodic deformations. To this end, we compare the measured force response of the actin cortex in HeLa cells in mitotic arrest to the simulated force response of elastic model cortices with known Poisson ratios (Fig. 1).

Because our goal is to measure the Poisson ratio of the actin cortex within live cells, we are not in a position to mechanically probe a work piece of cortical material in an arbitrary shape (such as a cylindrical work piece, which would allow the most direct measurement of the Poisson ratio (11)); the actin cortex in mitotic cells presents itself in the form of a thin cortical shell with a thickness of ~200 nm (12). Detection of shape changes of this cortical shell upon mechanical perturbation is hampered by the resolution of optical imaging (~200 nm) and the time dependence of viscoelastic cortex mechanics. In our approach, we circumvent these pitfalls by establishing that the contribution of cortical area dilation and area shear depend in a particular way on the elastic reference shape of the cortex. With this insight, we developed a scheme to extract two independent mechanical parameters of the actin cortex in mitotic HeLa cells—the area bulk modulus K_B and the area shear modulus K_S. We then infer the frequency-dependent Poisson ratio of the cortex from the relation $\nu = (K_B - K_S)/(K_B + K_S)$.

MATERIALS AND METHODS

Cell culture

We cultured HeLa Kyoto cells expressing a green-fluorescent histone construct (H2B-GFP) and red-fluorescent membrane label (mCherry-CAAX) in Dulbecco's modified Eagle's medium (PN:31966-021; Life Technologies, Carlsbad, CA) supplemented with 10% (vol/vol) fetal bovine serum, 100 μg/mL penicillin, 100 μg/mL streptomycin, and 0.5 μg/mL geneticin (all Invitrogen; Carlsbad, CA) at 37°C with 5% CO_2. 1 day before the measurement, 10,000 cells were seeded into a silicon cultivation chamber (0.56 cm^2, from ibidi 12 well chamber; Martinsried, Germany) that was placed in a 35 mm cell culture dish (FluoroDish FD35-100, glass bottom; World Precision Instruments, Sarasota, FL) such that a confluency of ~30% is reached at the day of measurement. For atomic force microscopy (AFM) experiments, medium was changed to Dulbecco's modified Eagle's medium (PN:12800-017; Invitrogen) with 4 mM $NaHCO_3$ buffered with 20 mM HEPES/NaOH (pH 7.2). Mitotic arrest of cells was achieved by addition of S-trityl-L-cysteine (Sigma-Aldrich, St. Louis, MO) 2–8 h before the experiment at a concentration of 2 μM. This allowed conservation of cell mechanical properties during measurement times of up to 30 min for one cell (13). Cells in mitotic arrest were identified by their shape and/or H2B-GFP. Diameters of uncompressed, roundish mitotic cells typically ranged from 19–23 μm.

AFM

The experimental setup consisted of an atomic force microscope (Nanowizard I; JPK Instruments, Bruker, Billerica, MA) mounted on a Zeiss Axiovert 200M optical wide-field microscope (Carl Zeiss, Oberkochen, Germany). For imaging, we used a 20× objective (Plan Apochromat, NA= 0.80; Carl Zeiss) and a CCD camera (DMK 23U445 from The Imaging Source, Bremen, Germany). During measurements, cell culture dishes were kept in a petri dish heater (JPK Instruments) at 37°C. On every measurement day, the spring constant of the cantilever was calibrated using the thermal noise analysis (built-in software; JPK Instruments). Cantilevers were tipless, 200–350 μm long, 35 μm wide, and 2 μm thick (NSC12/tipless/noAl or CSC37/tipless/noAl; Mikromasch, Wetzlar, Germany), with nominal force constants between 0.3 and 0.8 N/m. Cantilevers were modified with wedges to correct for the 10° cantilever tilt consisting of ultraviolet curing adhesive (63; Norland, Cranbury, NJ) (14). During

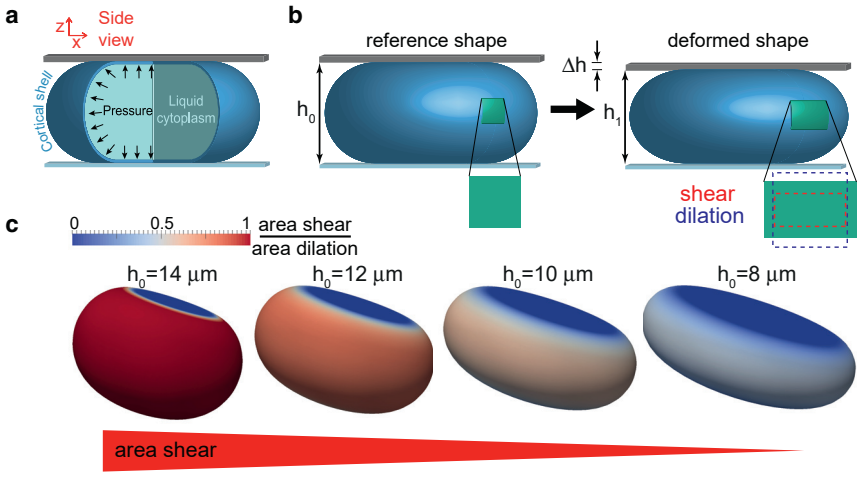

FIGURE 1 Elastic uniaxial compression of a cortical shell. (*a*) Cell-mechanical model is shown. (*b*) Left panel: a square-shaped surface element (*green*) in the elastic reference shape of the shell. Right panel: after a small amount of uniaxial compression through reduction of shell height, the surface element is deformed (deformation is exaggerated here for illustration purposes). (*c*) The elastic deformation of model cells exhibits a decreasing ratio of area shear/area dilation at decreasing reference cell heights (simulation parameters as in Fig. 2). To see this figure in color, go online.

measurements, measured force, piezo height, and time were outputted at a time resolution of 100Hz.

Cell compression protocol

Before cell compression, the atomic force microscope cantilever was lowered to the dish bottom near the cell until it came into contact with the surface and then retracted to ~15 μm above the surface. Thereafter, the free cantilever was moved over the cell. At this stage, a brightfield picture of the equatorial plane of the confined cell is recorded to estimate the area of the equatorial cross section and, in turn, to estimate cell volume as described in (2). The cantilever was then gradually lowered in steps of 0.5 or 1 μm at a set speed of 0.2 μm/s interrupted by waiting times of 50–150 s. During this waiting time, we performed sinusoidal oscillations around the mean cantilever height at different frequencies ($f = 0.02$, 0.1, 1, and 10 Hz), with a piezo height amplitude of 0.25 μm. The cycle of compression and subsequent oscillations around a constant mean height was repeated until the cell started to bleb, which was typically at a height of 10 μm. For frequencies $f = 0.1$–10 Hz, height oscillations were performed for ≥ 5 periods. For frequency $f = 0.02$ Hz, height oscillation were performed for ≥ 2 periods. For a first subset of cells ($N \approx 50$), mechanical probing was performed jointly at frequencies $f = 0.1$, 1, 10 Hz; for a second subset of cells ($N \approx 10$), all frequencies ($f = 0.02$, 0.1, 1, 10 Hz) were measured on one cell; and for a third subset of cells ($N \approx 25$), only the slow frequency of $f = 0.02$ Hz was measured to limit the overall measurement time on one cell. During the entire experiment, the force acting on the cantilever was continuously recorded. The height of the confined cell was computed as the difference between the height that the cantilever was raised from the dish surface and lowered onto the cell plus the height of spikes at the rim of the wedge (due to imperfections in the manufacturing process (14)) and the force-induced deflection of the cantilever. We estimate a total error of cell height of ~0.5 μm due to unevenness of the cantilever wedge and due to the vertical movement of the cantilever to a position above the cell.

Data analysis

Geometrical parameters of each analyzed cell (such as contact area A_c with the wedge, mean curvature H of the free cell surface, and cell surface area A) are for each cell, estimated as previously described in (2). Briefly, we estimated cell volume by the formula $V = -(\pi/24)h(h^2(3\pi - 10) - 6h(\pi - 4)R_{eq} - 24R_{eq}^2)$, which can be derived by approximating the profile of the free cell contour by a semicircle. Here, R_{eq} is the equatorial radius of the confined cell at confinement height h. Further, we estimated radii of principle curvatures at the equator of the cell surface as $h/2$ and R_{eq}. The area of contact between cells and cantilever was estimated as $A_c = \pi r_c^2$ with the contact radius r_c determined by the approximative formula $r_c = (R_{eq} - (h/2)) + (2/3)\left(\sqrt{(2R_{eq}^3 - hR_{eq}^2)}/\sqrt{(h + 2R_{eq})} - (R_{eq} - (h/2))\right)$ described in (15).

In turn, these parameters are used to calculate the effective cortical tension γ_{eff} according to Eq. 2.

Because we impose only small deformation oscillations on the cell, we may use an analysis scheme in the framework of linear viscoelasticity, as shown in our previous work (2; Supplementary Material). Oscillation amplitudes of effective cortical tension $\widehat{\gamma}_{eff}$ and cell surface area $\widehat{A}$ were determined by performing a linear fit using the fit function $a\cos(2\pi t/T) + b\sin(2\pi t/T) + c\,t$, where T is the oscillation period of the imposed cantilever oscillations. The oscillation amplitude was then calculated as $a^2 + b^2$. The strain amplitude $\widehat{\varepsilon}_A$ was calculated as $\widehat{A}/\langle A\rangle$.

For data analysis, only cells that had a roughly constant average cortical tension during the measurement (not more than 10% deviation) were considered. This was true for ~70% of the cells. Major variations in the cortical tension could mostly be attributed to visible blebbing events.

For the calculation of cortical Poisson ratios, we demanded that oscillatory measurements of cells had to be in a range of normalized height $\tilde{h}$ between 0.5 and 0.75 to match the parameters of the simulations. Only cells with at least four different heights sampled in this range were considered for analysis, in which the highest normalized height had to be larger than 0.68. Furthermore, we demanded that the r-squared value of the exponential fit of the obtained effective elastic modulus according to Eq. 5 had to be larger than 0.5. This constraint was released for Poisson ratio estimates larger than 0.7 because this indicates an almost constant value of effective modulus in dependence of cell height. For the case of a constant functional dependence, the fit cannot be better than the approximation of the data by the mean, leading to an r-squared value that approaches zero.

RESULTS

Theory of cortical shell deformation

Throughout this manuscript, we model the actin cortex of mitotic cells as a thin shell (Fig. 1 *a*). In the following section, we discuss the mechanics of thin shells and its dependence on the Poisson ratio of cortical shell material. We numerically determine the mechanical response of idealized model cells using established continuum mechanical concepts (11). The obtained insight is used to develop an analysis scheme that allows to extract the Poisson ratio of actin cortices from experimental data.

Our model cells are constituted by an isotropic contractile elastic thin shell mimicking the actin cortex, enclosing an incompressible liquid interior representing the cytoplasm (12). Cortical shells are thus assumed to enclose a constant volume V independent of elastic stresses because the associated hydrostatic pressures in the cell are negligible as compared to the osmotic pressure associated to the osmolarity of the medium (16). We assume a model shell thickness t_c of 200 nm, as measured before for the actin cortex of mitotic HeLa cells (12), and a model cell volume of $V = 4300\ \mu m^3$, which was approximately the average volume of mitotic HeLa cells in our experiments.

According to elasticity theory, the shell's elastic behavior is characterized by three elastic moduli: 1) the area bulk modulus K_B, characterizing the resistance to area dilation or compression; 2) the area shear modulus K_S, characterizing the resistance to shear deformation of a surface patch of the shell; and 3) the bending modulus B, characterizing the resistance to shell bending. In the case of an isotropic material, only two of the three moduli are independent, and we have $K_B = t_c G(1 + \nu)/(1 - \nu)$, $K_S = t_c G$, and $B = t_c^3 G/(12(1 - \nu))$, where G is the shear modulus of the shell (11,17).

Analogous to our experimental setup, we consider model cells that are confined between two parallel plates in an elastic reference configuration of height h_0; see Fig. 1, *a* and *b*. There, we anticipate a constant isotropic contractile in-plane stress σ_a in the cortical shell that captures active actomyosin contractility of the actin cortex, which gives

rise to a constant active cortical tension $\gamma_a = t_c\sigma_a$. This active tension is balanced by the internal hydrostatic pressure of the liquid interior. In the absence of elastic stresses, the contractile tension γ_a drives the model cell into the shape of an axisymmetric nonadherent droplet that is characterized by a constant mean curvature H in the regions of unsupported shell surface (15). We use these confined droplet shapes as the elastic reference configuration because the actin cortex has been previously characterized to be viscoelastic, with complete stress relaxations after ≤ 1 min (2). Therefore, mechanically confining cells to a height h leads to a new droplet-shaped reference shape of height h after a short waiting time. In this elastic reference state, a model cell exerts a constant force because of active tension

$$F_a(h) = 2\gamma_a H(h) A_c(h) \tag{1}$$

on the confining plates, where $A_c(h)$ is the circular contact area between the cell and the plate and H is the mean curvature, both at height h of the cell (2,15).

This force exerted on the confining plates is the central quantity of our investigations because we can measure it in our experiments and compute it in our finite element simulations (18). To probe the force response of a model cell, steps of uniaxial compression are imposed that lower the cell height from a starting height h_0 to $h_1 = h_0 - \Delta h$. In turn, the shell material is deformed, and elastic stresses are induced (Fig. 1, *a* and *b*). Together with an increase of the shell's plate contact, this contributes to an increase of the force exerted on the confining plates. The new force for the decreased plate distance h_1 is denoted as $F_{tot}(h_0, \Delta h) = F_a(h_1) + \Delta F(h_0, \Delta h)$, where $\Delta F(h_0, \Delta h)$ captures the elastic contribution of the force increase and $F_a(h_1)$ captures the force contribution from active tension at new height h_1. For our study, we consider small compression steps in which $\Delta F(h_0, \Delta h)$ is well approximated as a linear function of Δh. Furthermore, we verified in numerical simulations that the force response of the liquid interior adds $\leq 1\%$ to the effective modulus for cytoplasmic viscosities of up to 1 Pa • s, oscillation frequencies ≤ 10 Hz (see Supporting Materials and Methods, Section 2), and normalized cell height lower than 80%. Therefore, we henceforth neglect viscous flows in the cytoplasm, simulating only the elastic deformation of a shell and an internal pressure.

In analogy to Eq. 1, we can relate the overall force of the cortex after elastic deformation to an effective cortical tension (2)

$$\gamma_{eff}(h_0, \Delta h) = \frac{F_{tot}(h_0, \Delta h)}{2H(h_1)A_c(h_1)}, \tag{2}$$

where $\gamma_{eff} = \gamma_a + \Delta\gamma_{eff}$, with $\Delta\gamma_{eff} = \Delta F(h_0, \Delta h)/(2H(h_1)A_c(h_1))$. Here, γ_a captures the constant active contribution to cortical tension, whereas $\Delta\gamma_{eff}$ denotes the passive deformation-induced tension change.

We define an effective elastic modulus of uniaxial shell compression as

$$K(h) = \frac{\Delta\gamma_{eff}}{\varepsilon_A}, \tag{3}$$

where $h = (h_0 + h_1)/2$ and ε_A is the surface area strain

$$\varepsilon_A = \Delta A(h_0, \Delta h)/A(h_0), \tag{4}$$

with ΔA the increase in overall surface area of the model cell through deformation and $A(h_0)$ the original surface area at height h_0 in the absence of elastic stresses (2).

We determined values of $K(h)$ of shells of known mechanical properties via simulations of thin-shell continuum mechanics (Fig. 2 *b*; (19)).

Finite element simulations were carried out to extract the effective elastic modulus $K(h)$ for 540 combinations of cell heights, area shear moduli, bending stiffnesses, and surface tensions (see Supporting Materials and Methods, Sections 3 and 4). For convenience, we introduce now the normalized cell height $\tilde{h} = h/(2R)$ with $R = ((3/4\pi)V)^{1/3}$. We find that at low values of normalized reference cell height $\tilde{h}$, the effective modulus K approaches the area bulk modulus K_B because of the dominance of area dilation over area shear during shell deformation (Fig. 2, *a* and *b*). For larger normalized heights $\tilde{h}$, the effective modulus K increases because of an increasing contribution of area shear during model cell deformation (Fig. 2 *b*). We can capture this increase phenomenologically by an exponential rise

$$K(\tilde{h}) \approx K_B\left(1 + \alpha \exp\left(\tilde{h}/\lambda\right)\right), \tag{5}$$

where $\lambda \approx 0.09$ (*dashed lines* in Fig. 2 *b*; see Supporting Materials and Methods, Section 3). The amplitude of the exponential increase α depends on the normalized shear modulus $\tilde{K}_S = K_S/K_B$ as well as the normalized surface tension $\tilde{\gamma}_a = \gamma_a/K_B$. In the experimentally relevant range $0.45 < \tilde{h} < 0.75$, we capture this dependence again by a phenomenological law

$$\alpha(\tilde{K}_S, \tilde{\gamma}_a) \approx C(\tilde{\gamma}_a)\log\left[\tilde{K}_S\right] + D(\tilde{\gamma}_a), \tag{6}$$

where $C(\tilde{\gamma}_a)$ and $D(\tilde{\gamma}_a)$ are polynomials of the third degree in $\tilde{\gamma}_a$ (*dashed lines* in Fig. 2 *c*; Supporting Materials and Methods, Section 3).

The characterizing Eqs. 5 and 6 provide now an analysis scheme to extract the Poisson ratio from measured effective moduli $K(\tilde{h})$ for known γ_a (Fig. 3 *a*): fitting an exponential increase to $K(\tilde{h})$ yields fit parameters α and K_B (compare Eq. 5). Inverting the function (6) at α numerically, an estimate of $\tilde{K}_S$ is obtained that, in turn, allows us to determine the Poisson ratio by $\nu = (1 - \tilde{K}_S)/(1 + \tilde{K}_S)$. As a test of self-consistency, we verified that the application of this analysis scheme closely reproduces the chosen values of the

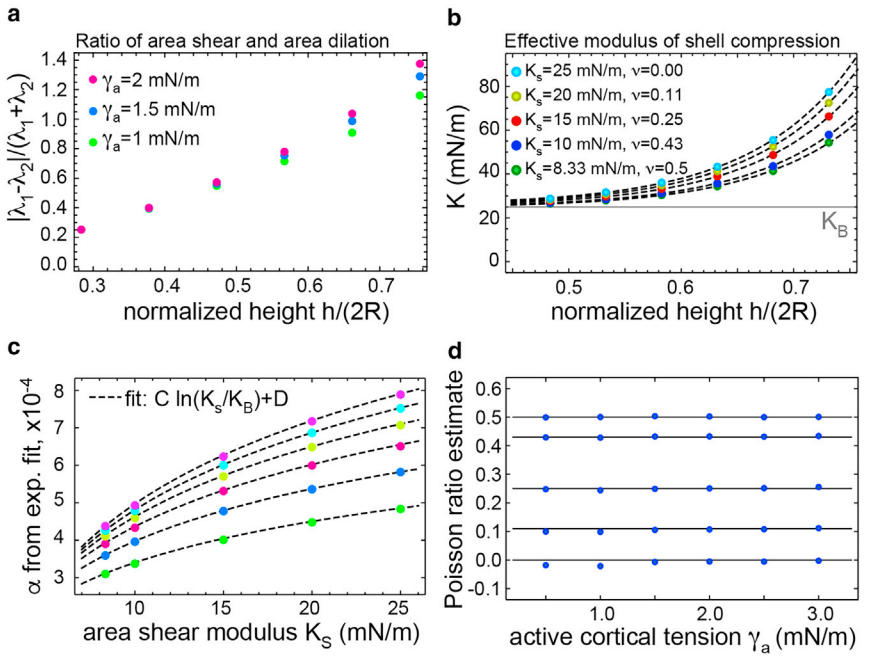

FIGURE 2 Uniaxial compression of elastic model cells with varying reference height. (*a*) Ratio of area shear/area dilation at the shell equator is quantified as $|\lambda_1 - \lambda_2|/(\lambda_1 + \lambda_2)$, where λ_1 and λ_2 are the equatorial eigenvalues of the in-plane shear tensor. (*b*) Effective elastic modulus K is shown as a function of mean shell height $h = h_0 - \Delta h/2$ for cortical tension $\gamma_a = 1.5$ mN/m (*dashed lines*: fitted by Eq. 5). The numerical uncertainty of K was estimated to be $\leq 0.4\%$. (*c*) Fit coefficient α is shown as a function of K_S for varying cortical tensions γ_a (*bottom* to *top*: 0.5–3 mN/m in increments of 0.5 mN/m, *dashed lines*: fitted by Eq. 6). The choice of cortical tension reflects the range of experimental values. (*d*) Reconstructed Poisson ratios (*blue dots*) from effective elastic moduli are as shown in (*b*). Black lines indicate actual Poisson ratio values of underlying simulations. Elastic parameters were chosen to be $K_B = 25$ mN/m and $K_S = 8.3$, 10, 15, 20, or 25 mN/m, corresponding to Poisson ratios of $\nu = 0.5$, 0.43, 0.25, 0.11, and 0. Values of K_B were motivated by measurement results reported by (2). The cell volume was 4300 μm^3, and $\Delta h = 0.5$ μm. To see this figure in color, go online.

Poisson ratio for model cells (Fig. 2 *d*). Thus, the exponential increase of the effective elastic modulus K as a function of $\tilde{h}$ stores the information about the Poisson ratio of the shell.

Experimental results

We now want to use our theoretical insight to determine the Poisson ratio of the actin cortex in live cells. As a cellular model system, we use HeLa cells in mitotic arrest because they are void of a nucleus and exhibit a large cell surface tension that ensures droplet-shaped cells in confinement (15). Furthermore, for mitotic cells, we could show in a previous study that the actin cortex is the dominant mechanical structure and that the influence of cell adhesion is negligible in our measurement setup (2,15).

We mechanically deform these cells in an oscillatory manner around different heights of confinement via the wedged cantilever of an atomic force microscope (Fig. 3 *b*; (2,15)). During these measurements, we record the force exerted by the atomic force microscope cantilever and the respective cantilever height h_{cant} (Fig. 3 *c*). We then calculate the associated time-periodic effective cortical tension $\gamma_{eff}(t)$ and area strain $\varepsilon_A(t)$ according to Eqs. 2 and 4 with $h_1(t) = h_{cant}(t)$, $h = <h_{cant}(t)>$, and $\Delta h(t) = h_1(t) - h$ (Fig. 3 *d*). We determine the volume of the measured cell V from imaging and calculate an associated cell radius R (see Materials and Methods). In analogy to Eq. 3, we infer an effective modulus of the actin cortex of measured cells $K = (\hat{\gamma}_{eff}/\hat{\varepsilon}_A)$, where $\hat{\gamma}_{eff}$ and $\hat{\varepsilon}_A$ are the amplitudes of the time-periodic signal of γ_{eff} and $\varepsilon_A = \Delta A/\langle A \rangle$, respectively (Fig. 3 *d*; (2)). Our measurement and analysis procedure is repeated at different cell heights to obtain K as a function of normalized cell confinement height $\tilde{h}$ (Fig. 3, *e* and *f*).

Cell mechanical measurements are performed at frequencies 0.02, 0.1, 1, and 10 Hz. Using the correspondence principle, we apply our insight on the mechanical response of elastic model cells to our measurements of viscoelastic live cells (20): we fit the measured height dependence of the cortical modulus K by Eq. 5 and obtain the fit parameter α and K_B (Fig. 3 *f*). In general, we find a good agreement between measured values and the exponential increase predicted by our elastic shell calculations with a median r-squared value of 0.94 for $f = 0.1$–10 Hz and 0.84 for $f = 0.02$ Hz. The good agreement between data points and the fitting function provided by numerical simulation illustrates the suitability of our cell mechanical description.

Furthermore, we estimate the cortical tension as the time-average $\gamma_a \approx <\gamma_{eff}>$. Inverting Eq. 6, we obtain an estimate for $\tilde{K}_S = K_S/K_B$ and thus the Poisson ratio ν (Fig. 4, *a*–*c*; Fig. S3, *a* and *b*). We find that the obtained Poisson ratio estimate depends on the frequency of time-periodic cell deformations, with lower Poisson ratios for fast cell deformations. Median values of the Poisson ratio vary between values of 0.17 and 0.48 for decreasing frequencies between 10 and 0.1 Hz (Fig. 4, *c* and *d*). For the slowest frequency 0.02 Hz, at which cortex turnover is expected to influence cell mechanics, we estimate a median Poisson ratio of 0.66 (Fig. 4, *c* and *d*).

Our results show a substantial scatter of Poisson ratio estimates at a given frequency (Fig. 4 *c*). To examine the origin of this statistical spread, we quantify the influence of experimental uncertainties. To this end, we assess the error of our cell volume estimate to be 7.5% and of cell height to be 0.5 μm. In turn, we calculate the resulting

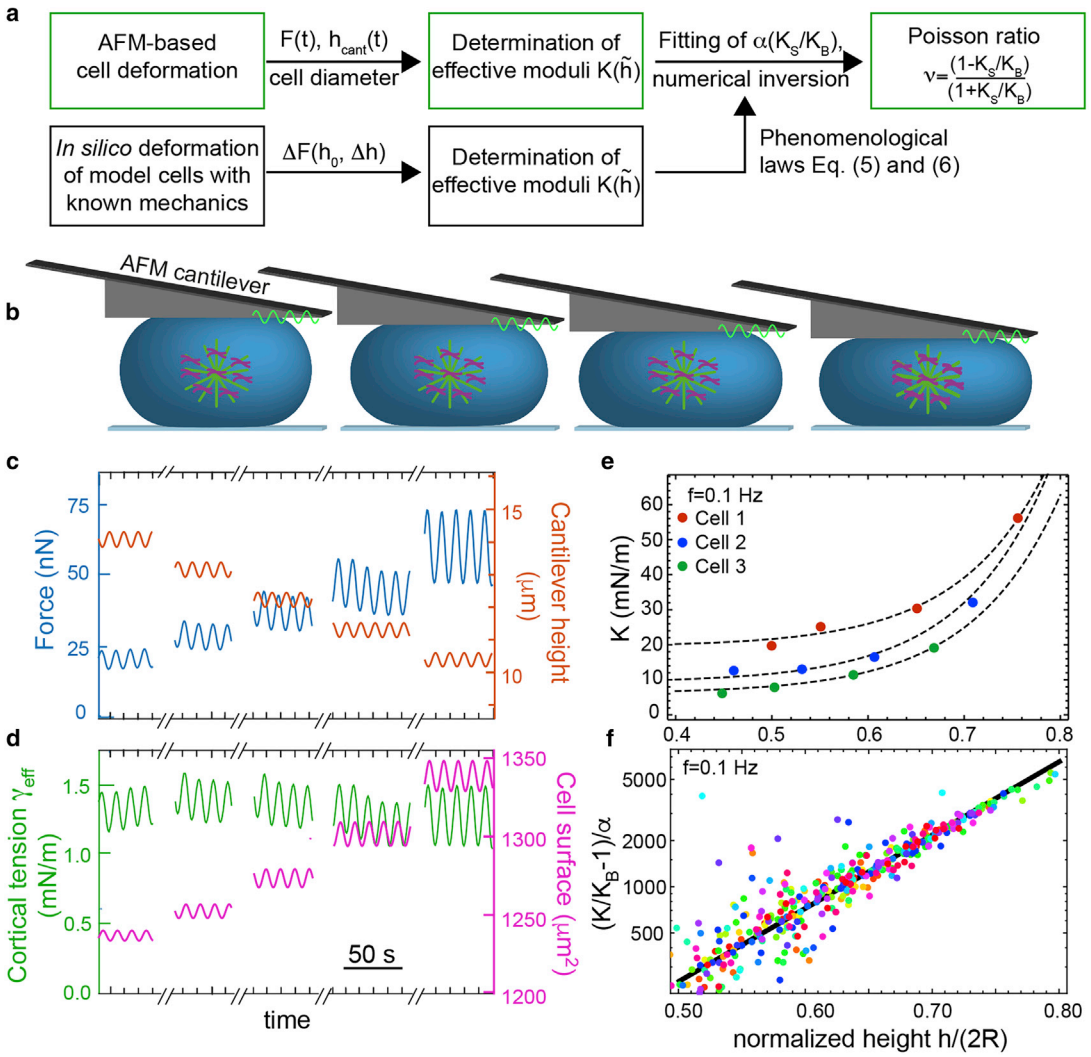

FIGURE 3 AFM-based deformation of HeLa cells. (*a*) A scheme of data analysis workflow is given. (*b*) Cells in mitotic arrest were confined through a wedged cantilever (schematic: *green*, microtubules; *violet*, chromosomes). Oscillatory cell height modulations are applied at decreasing mean cell heights. (*c*) Exemplary force and cantilever height output at $f = 0.1$ Hz is shown. (*d*) Values of cortical tension and cell surface area associated with (*c*) were calculated from force and cantilever height as described before in (2). (*e*) Exemplary effective elastic moduli of cell cortices versus normalized cell heights is shown. Dashed lines show a fit according to Eq. 5 with fit parameters K_B and α. Uncertainties of estimated moduli because of sinusoidal fitting of output tension data are estimated to be $\leq 5\%$. (*f*) Normalized effective elastic moduli $(K/K_B - 1)/\alpha$ of all cells measured at $f = 0.1$ Hz is shown. The phenomenological dependence predicted by Eq. 5 is captured by the solid black line. Different colors represent different cells. To see this figure in color, go online.

variation of Poisson ratios for elastic model cells with a known Poisson ratio by introducing corresponding artificial errors in cell volume and cell height (see Fig. S3 *c*). In this way, we find resulting interquartile ranges (IQRs) between 0.24 and 0.39, which are close to IQR values found for experimental spreads. Therefore, we conclude that statistical scatter in our experimental data stems a substantial amount from measurement errors and not exclusively from cell-cell variations.

Among cell-cell variations, we expect variations in cortical thickness and thus in the contribution of bending stiffness to cell deformations as a major source for variations in Poisson ratio estimates (see Supporting Materials and Methods, Section 6). In summary, despite large statistical scatter, we observe a robust, significant trend of increasing Poisson ratio values of the mitotic actin cytoskeleton with decreasing frequency (Fig. 4, *c* and *d*) in which Poisson ratio distributions are significantly different from each other at different frequencies (two-sided Mann-Whitney test: p-values ≤ 0.02 for neighboring frequencies, $\leq 10^{-4}$ for all other frequency pairs).

DISCUSSION

Here, we report a new measurement method to determine the Poisson ratio of the actin cortex in biological cells that is based on the time-periodic deformation of initially round mitotic cells through the wedged cantilever of an atomic

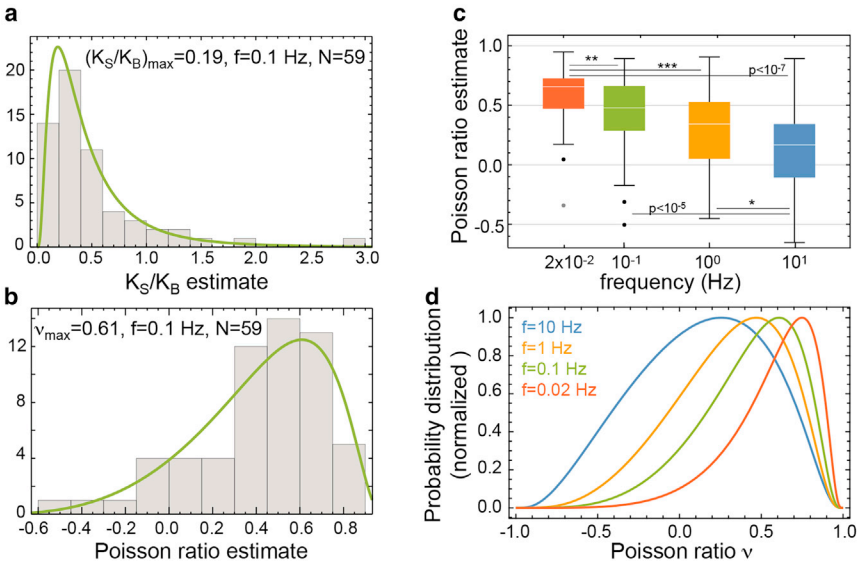

FIGURE 4 Poisson ratio estimates of the actin cortex in mitotic HeLa cells. (*a*) A histogram of estimated K_S/K_B at $f = 0.1$ Hz (*green line* represents lognormal distribution of maximal likelihood) is given. (*b*) A histogram of corresponding Poisson ratios is given (*green line*: distribution induced by lognormal distribution in *a*). (*c*) Box plots of estimated Poisson ratios at different frequencies are given. From left to right, median values: 0.66, 0.48, 0.34, 0.17; IQR: 0.26, 0.38, 0.48, 0.45. Stars indicate significant differences between distributions according to *p*-values of a Mann-Whitney test ($*p < 0.05$, $**p < 0.01$, $***p < 0.001$). (*d*) Fitted distributions of estimated Poisson ratios for cell deformations at frequencies $F = 0.02$, 0.1, 1, and 10 Hz are shown. To see this figure in color, go online.

force microscope. The key idea behind this technique is that mechanical deformation at different reference shapes probes the cortical shell at varying contributions of area dilation and area shear (Figs. 1, *b* and *c* and 2 *a*).

For our measurements at the largest frequency ($f = 10$ Hz), we expect that cortex turnover plays a negligible role for the mechanical properties of the cortex (1). There, we find a median Poisson ratio of 0.17. This value is considerably lower than the incompressible case of $\nu = 0.5$ and reasonably close to theoretical predictions of 0.25 for foamed elastic materials or polymer gels (21,22).

Furthermore, we find a clear trend for the Poisson ratio to increase with timescale; median values of the Poisson ratio increase from 0.17 to 0.66 in a timescale range of $\tau \approx 0.016$–8 s, associated with a frequency range of $f = 0.02$–10 Hz by $\tau = 1/(2\pi f)$ (Fig. 4, *c* and *d*). A plausible explanation for this trend is that turnover of actin and, in particular, actin cross-linkers (taking place on timescales of ~0.2–20 s (1)) leads to a significant decrease of the shear modulus at increasing timescales. For cross-linker turnover, this effect has been demonstrated by Broedersz et al. (23). On the other hand, turnover supposedly gives rise to a minor change of the bulk modulus of the cortex because the actin polymer density is preserved. Correspondingly, the Poisson ratio would decrease with timescale and increase with frequency (for an elastic isotropic material with shear modulus G and bulk modulus $\mathcal{K}$, the Poisson ratio is given by $\nu = (3\mathcal{K}/G - 2)/(6\mathcal{K}/G + 2)$. If $\mathcal{K}/G$ increases, ν increases and approaches 0.5 for large $\mathcal{K}/G$). Indeed, a similar effect was reported as a hallmark for the glass transition of synthetic polymer materials (9). There, an increase of Poisson ratio as a function of timescale was reported when moving from glassy to rubbery rheological behavior. Correspondingly, this transition is accompanied by a strong decrease of the shear modulus because of jamming release but a minor decrease of the bulk modulus with timescale (9,10,24).

It is noteworthy that for a thin shell of an isotropic material, the associated two-dimensional Poisson ratio ν_{2d} coincides with the three-dimensional Poisson ratio ν. In this case, ν_{2d} may adopt values in the range $[-1, 0.5]$ (see Supporting Materials and Methods, Section 7). However, if the assumption of material isotropy is relaxed, ν_{2d} may adopt values that may reach up to 1. For the slowest frequency probed in our measurements, the Poisson ratio estimate exceeds 0.5. This might hint at a violation of cortical isotropy at slower frequencies. Cortical turnover is critically influenced by the cortex interface with the plasma membrane (1,25), which might account for the emergence of anisotropy at large timescales.

Poisson ratios of cellular material have been previously estimated: Mahaffy et al. developed a method to estimate the Poisson ratio of adherent cells through slow atomic force microscope indentation at a gradually increasing indentation depth into a thin cytoskeletal layer above a substrate (26). Poisson ratio estimates from this method are between 0.4 and 0.5 (26–28). Trickey et al. (29) measured the Poisson ratio of chondrocytes through a whole-cell perturbation via micropipette aspiration and subsequent shape relaxation, thereby estimating values of 0.38. However, both methods (26,29) ignored the possible timescale dependence of the Poisson ratio. This fact makes it hard to compare these earlier findings to our data. We do, however, anticipate that our measurement results do not contradict with those previous measurements because of our comparable results in the frequency range 0.1–1 Hz.

For in vitro reconstituted branched actin meshworks, Bussonnier et al. clearly showed the compressibility of branched actin meshworks on a timescale of a few seconds (Poisson ratio between 0.1 and 0.2) (30). By contrast, entangled actin meshworks without cross-linking were shown to be close to incompressible (31). This discrepancy indicates that not

only the timescale but also the presence of actin cross-linkers plays a crucial role for the Poisson ratio of actin meshworks.

To the best of our knowledge, we present here for the first time measurements of the Poisson ratio of the actin cortex in live cells independent of frequency, showing a clear frequency-dependent trend. In particular, our measurements indicate a nonmonotonic dependence of cortical Poisson ratio on timescale: for very short timescales, poroelastic effects and incompressibility of water will give rise to a decrease of Poisson ratio with timescale (see Supporting Materials and Methods, Section 1). At larger timescales, at which turnover of cortical constituents starts to kick in, there is an increase of the Poisson ratio with timescale. In summary, we give evidence that the actin cortex may not in general be treated as an incompressible material. Therefore, compression or dilation of the actin cytoskeleton is possible in response to acting forces at sufficiently fast timescales. In particular, local compression of actin cytoskeleton may be caused by motor-induced cytoskeletal contractility, which would, in turn, increase myosin motor concentration locally. This may contribute to a self-amplifying effect that could induce instability and pattern formation in the material (17,32–34). Our results therefore make a contribution to the parameterization of active gel theory and mechanical modeling of the dynamics of the actin cytoskeleton (35,36).

SUPPORTING MATERIAL

Supporting Material can be found online at https://doi.org/10.1016/j.bpj.2020.03.002.

AUTHOR CONTRIBUTIONS

S.A. and E.F.-F. designed the research. M.M. and S.A. developed the numerical method. M.M. performed simulations. K.H. and E.F.-F. performed the experiments. M.M., K.H. and E.F.-F. performed data analysis. M.M., S.A., and E.F.-F. wrote the manuscript.

ACKNOWLEDGMENTS

We thank Jochen Guck, Isabel Richter, and Anna Taubenberger for access and introduction to infrastructure in the lab. In addition, we thank the Center for Molecular and Cellular Bioengineering light microscopy facility for excellent support.

S.A. acknowledges support from the Deutsche Forschungsgemeinschaft (grant AL 1705/3) and tax money based on the budget passed by the delegates of the Saxonian state parliament. E.F.-F. thanks for financial support from the Deutsche Forschungsgemeinschaft, project FI 2260/4-1. S.A. and E.F.-F. acknowledge financial support from the Deutsche Forschungsgemeinschaft in the context of the Forschergruppe FOR3013, projects AL 1705/6-1 (S.A.) and FI 2260/5-1 (E.F.-F.). Simulations were performed at the Center for Information Services and High Performance Computing at Technische Universität Dresden.

SUPPORTING CITATIONS

References (37–43) appear in the Supporting Material.

REFERENCES

1. Salbreux, G., G. Charras, and E. Paluch. 2012. Actin cortex mechanics and cellular morphogenesis. *Trends Cell Biol.* 22:536–545.
2. Fischer-Friedrich, E., Y. Toyoda, …, F. Jülicher. 2016. Rheology of the active cell cortex in mitosis. *Biophys. J.* 111:589–600.
3. Pullarkat, P. A., P. A. Fernández, and A. Ott. 2007. Rheological properties of the Eukaryotic cell cytoskeleton. *Phys. Rep.* 449:29–53.
4. Kollmannsberger, P., and B. Fabry. 2011. Linear and nonlinear rheology of living cells. *Annu. Rev. Mater. Res.* 41:75–97.
5. Jülicher, F., K. Kruse, …, J. F. Joanny. 2007. Active behavior of the cytoskeleton. *Phys. Rep.* 449:3–28.
6. Dimitriadis, E. K., F. Horkay, …, R. S. Chadwick. 2002. Determination of elastic moduli of thin layers of soft material using the atomic force microscope. *Biophys. J.* 82:2798–2810.
7. Koenderink, G. H., M. Atakhorrami, …, C. F. Schmidt. 2006. High-frequency stress relaxation in semiflexible polymer solutions and networks. *Phys. Rev. Lett.* 96:138307.
8. Fabry, B., G. N. Maksym, …, J. J. Fredberg. 2001. Scaling the microrheology of living cells. *Phys. Rev. Lett.* 87:148102.
9. Greaves, G. N., A. L. Greer, …, T. Rouxel. 2011. Poisson's ratio and modern materials. *Nat. Mater.* 10:823–837.
10. Lu, H., X. Zhang, and W. G. Knauss. 1997. Uniaxial, shear, and Poisson relaxation and their conversion to bulk relaxation: studies on poly(-methyl methacrylate). *Polym. Eng. Sci.* 18:211–222.
11. Landau, L., and E. Lifshitz. 1986. Theory of Elasticity, Third Edition. Elsevier Ltd, Oxford.
12. Clark, A. G., K. Dierkes, and E. K. Paluch. 2013. Monitoring actin cortex thickness in live cells. *Biophys. J.* 105:570–580.
13. Skoufias, D. A., S. DeBonis, …, F. Kozielski. 2006. S-trityl-L-cysteine is a reversible, tight binding inhibitor of the human kinesin Eg5 that specifically blocks mitotic progression. *J. Biol. Chem.* 281:17559–17569.
14. Stewart, M. P., A. W. Hodel, …, J. Helenius. 2013. Wedged AFM-cantilevers for parallel plate cell mechanics. *Methods.* 60:186–194.
15. Fischer-Friedrich, E., A. A. Hyman, …, J. Helenius. 2014. Quantification of surface tension and internal pressure generated by single mitotic cells. *Sci. Rep.* 4:6213.
16. Clark, A. G., and E. Paluch. 2011. Mechanics and regulation of cell shape during the cell cycle. *In* Cell Cycle in Development. J. Z. Kubiak, ed. Springer, pp. 31–73.
17. Berthoumieux, H., J.-L. Maître, …, G. Salbreux. 2014. Active elastic thin shell theory for cellular deformations. *New J. Phys.* 16:065005.
18. Mokbel, M., D. Mokbel, …, S. Aland. 2017. Numerical simulation of real-time deformability cytometry to extract cell mechanical properties. *ACS Biomater. Sci. Eng.* 3:2962–2973.
19. Mokbel, M., and S. Aland. 2019. An ALE method for simulations of axisymmetric elastic surfaces in flow. *arXiv*, arXiv:1912.04899 https://arxiv.org/abs/1912.04899.
20. Lakes, R. S. 2017. Viscoelastic Solids (1998). CRC Press, Boca Raton, FL.
21. Gent, A. N., and A. G. Thomas. 1959. The deformation of foamed elastic materials. *J. Appl. Polym. Sci.* 1:107–113.
22. Geissler, E., and A. M. Hecht. 1980. The Poisson ratio in polymer gels. *Macromolecules.* 13:1276–1280.
23. Broedersz, C. P., M. Depken, …, F. C. MacKintosh. 2010. Cross-link-governed dynamics of biopolymer networks. *Phys. Rev. Lett.* 105:238101.
24. Tschoegl, N. W., W. G. Knauss, and I. Emri. 2002. Poisson's ratio in linear viscoelasticity – a critical review. *Mech. Time-Depend. Mater.* 6:3–51.
25. Charras, G. T., C.-K. Hu, …, T. J. Mitchison. 2006. Reassembly of contractile actin cortex in cell blebs. *J. Cell Biol.* 175:477–490.

26. Mahaffy, R. E., S. Park, …, C. K. Shih. 2004. Quantitative analysis of the viscoelastic properties of thin regions of fibroblasts using atomic force microscopy. *Biophys. J.* 86:1777–1793.

27. Betz, T., D. Koch, …, J. A. Käs. 2011. Growth cones as soft and weak force generators. *Proc. Natl. Acad. Sci. USA.* 108:13420–13425.

28. Lu, Y.-B., T. Pannicke, …, A. Reichenbach. 2013. Biomechanical properties of retinal glial cells: comparative and developmental data. *Exp. Eye Res.* 113:60–65.

29. Trickey, W. R., F. P. T. Baaijens, …, F. Guilak. 2006. Determination of the Poisson's ratio of the cell: recovery properties of chondrocytes after release from complete micropipette aspiration. *J. Biomech.* 39:78–87.

30. Bussonnier, M., K. Carvalho, …, T. Betz. 2014. Mechanical detection of a long-range actin network emanating from a biomimetic cortex. *Biophys. J.* 107:854–862.

31. Gardel, M. L., M. T. Valentine, …, D. A. Weitz. 2003. Microrheology of entangled F-actin solutions. *Phys. Rev. Lett.* 91:158302.

32. Mietke, A., V. Jemseena, …, F. Jülicher. 2019. Minimal model of cellular symmetry breaking. *Phys. Rev. Lett.* 123:188101.

33. Mietke, A., F. Jülicher, and I. F. Sbalzarini. 2019. Self-organized shape dynamics of active surfaces. *Proc. Natl. Acad. Sci. USA.* 116:29–34.

34. Bois, J. S., F. Jülicher, and S. W. Grill. 2011. Pattern formation in active fluids. *Phys. Rev. Lett.* 106:028103.

35. Prost, J., F. Jülicher, and J.-F. Joanny. 2015. Active gel physics. *Nat. Phys.* 11:111–117.

36. Joanny, J.-F., and J. Prost. 2009. Active gels as a description of the actin-myosin cytoskeleton. *HFSP J.* 3:94–104.

37. Biot, M. A., and D. G. Willis. 1957. The elastic coefficients of the theory of consolidation. *J. Appl. Mech.* 24:594–601.

38. Granger, R. A. 2012. Fluid Mechanics. Courier Corporation, Chelmsford, MA.

39. Kalwarczyk, T., N. Ziębacz, …, R. Hołyst. 2011. Comparative analysis of viscosity of complex liquids and cytoplasm of mammalian cells at the nanoscale. *Nano Lett.* 11:2157–2163.

40. Valentine, M. T., Z. E. Perlman, …, D. A. Weitz. 2005. Mechanical properties of Xenopus egg cytoplasmic extracts. *Biophys. J.* 88:680–689.

41. Witkowski, T., S. Ling, …, A. Voigt. 2015. Software concepts and numerical algorithms for a scalable adaptive parallel finite element method. *Adv. Comput. Math.* 41:1145–1177.

42. Mokbel, D., H. Abels, and S. Aland. 2018. A phase-field model for fluid-structure interaction. *J. Comput. Phys.* 372:823–840.

43. Hu, W.-F., Y. Kim, and M.-C. Lai. 2014. An immersed boundary method for simulating the dynamics of three-dimensional axisymmetric vesicles in Navier–Stokes flows. *J. Comput. Phys.* 257:670–686.

Biophysical Journal, Volume *118*

Supplemental Information

The Poisson Ratio of the Cellular Actin Cortex Is Frequency Dependent

Marcel Mokbel, Kamran Hosseini, Sebastian Aland, and Elisabeth Fischer-Friedrich

Supporting material:
The Poisson ratio of the cellular actin cortex is frequency-dependent

M. Mokbel,[1] K. Hosseini,[2,3] S. Aland,[1, a)] and E. Fischer-Friedrich[2, 3, b)]
[1)] *Faculty of Informatics/Mathematics, Hochschule für Technik und Wirtschaft, Dresden, Germany*
[2)] *Cluster of Excellence Physics of Life, Technische Universität Dresden, Dresden, Germany*
[3)] *Biotechnology Center, Technische Universität Dresden, Dresden, Germany*

I. EFFECTIVE COMPRESSION MODULUS OF A THIN POROELASTIC LAYER

In the following, we estimate an effective bulk modulus of a fluid-filled elastic scaffold taking into account fluxes of the fluid relative to the scaffold. We show that poroelastic effects likely affect compressibility of the actin cytoskeleton only for frequencies significantly higher than 10 Hz.
For a poroelastic material consisting of a viscoelastic porous scaffold and an immersing fluid, we have in Cartesian coordinates[1]

$$\epsilon_{ii} = \frac{1}{K}\left(\frac{\sigma_{ii}}{3} + p_H\right), \tag{1}$$

where p_H is the hydrostatic pressure increment in the fluid, K is the bulk modulus of the scaffold material, and σ_{ij} and ϵ_{ij} are the components of the stress and strain tensor of the elastic scaffold, respectively. Using Darcy's law, one obtains[1]

$$\frac{k_{perm}}{\eta}\Delta p_H = \frac{\partial \epsilon_{ii}}{\partial t}, \tag{2}$$

where k_{perm} characterizes the permeability of the scaffold material, η is the viscosity of the immersing fluid and Δ is the Laplace operator. Consider a flat horizontal layer of porous material with thickness t_c. We choose the middle layer of the layer to be at coordinate $z = 0$. Consider that oscillating opposing uniform forces are applied at the top and the bottom of the layer by a porous slab such that a small time-periodic (sinusoidal) compression is achieved. The edges of the layer are clamped such that displacement in x- and y-direction are prohibited. In this case, the trace of the strain tensor is $\epsilon_{ii} = \epsilon_{zz}$. Equivalently, $\sigma_{ii} = \sigma_{zz}$, where σ_{zz} varies time-periodically but is spatially uniform due to the force balance requirement $\partial_z \sigma_{zz} = 0$. According to Eqn. (1) and (2), we have $\epsilon_{zz} = \frac{1}{K}(\frac{\sigma_{zz}}{3} + p_H)$ and $i\omega\epsilon_{zz} = \frac{k_{perm}}{\eta}\partial_z^2 p_H$, where we identified the time-derivative with a multiplication by $i\omega$. We therefore obtain the following partial differential equation in p_H

$$\frac{i\omega}{K}\left(\frac{\sigma_{zz}}{3} + p_H\right) = \frac{k_{perm}}{\eta}\partial_z^2 p_H. \tag{3}$$

A special solution of Eq. (3) is $p_H = -\sigma_{zz}/3$. The general solution of the corrsponding homogeneous equation reads $p_H^h(z) = Ae^{\frac{z}{\lambda}} + Be^{-\frac{z}{\lambda}}$, where $\lambda = \sqrt{\frac{Kk_{perm}}{i\omega\eta}}$. Assuming that the porosity of the confining slabs is significantly larger than the porosity of the poroelastic layer, we impose the boundary conditions[1] $p_H(z = \pm t_c/2) = 0$ and obtain the full solution

$$p_H(t, z) = \frac{\sigma_{zz}(t)}{3}\left(\frac{(e^{\frac{z}{\lambda}} + e^{-\frac{z}{\lambda}})}{(e^{\frac{t_c}{2\lambda}} + e^{-\frac{t_c}{2\lambda}})} - 1\right) \tag{4}$$

For the strain, we find

$$\epsilon_{zz}(t, z) = \frac{\sigma_{zz}}{3K}\frac{(e^{\frac{z}{\lambda}} + e^{-\frac{z}{\lambda}})}{(e^{\frac{t_c}{2\lambda}} + e^{-\frac{t_c}{2\lambda}})} \tag{5}$$

[a)] Electronic mail: Corresponding author: sebastian.aland@htw-dresden.de
[b)] Electronic mail: Corresponding author: elisabeth.fischer-friedrich@tu-dresden.de

Accordingly, we obtain for the displacement component in z-direction

$$u_z(t,z) = \frac{\sigma_{zz}\lambda}{3K}\frac{(e^{\frac{z}{\lambda}} - e^{-\frac{z}{\lambda}})}{(e^{\frac{t_c}{2\lambda}} + e^{-\frac{t_c}{2\lambda}})}, \tag{6}$$

For large λ, the displacement at the boundary $z = t_c/2$ can be rewritten as

$$u_z(z = t/2) = \frac{\sigma_{zz}}{3K\left(1 + \frac{t_c^2}{12\lambda^2}\right)}\frac{t_c}{2} + \mathcal{O}(\frac{1}{\lambda^4}), \tag{7}$$

where $\mathcal{O}$ denotes the Landau symbol. Therefore, we may infer an effective compression modulus of the form

$$K_{eff} = K\left(1 + \frac{t_c^2}{12\lambda^2}\right) = \left(K + \frac{i\omega\eta t_c^2}{12k_{perm}}\right).$$

The absolute value of K_{eff} grows with frequency reflecting a trend to approach an effective incompressibility in the large frequency regime.

In the following, we will give a rough order of magnitude estimate of the dissipative term $\frac{i\omega\eta t_c^2}{12k_{perm}}$ in K_{eff} for parameters of the actin cortex layer in mitotic cells. Based on the Hagen-Poiseuille equation[2], we estimate the permeability of the actin cytoskeleton as $d_{pore}^2/32$, where d_{pore} is the diameter of a cytoskeletal pore which we assume to be $\approx 50\,\mathrm{nm}$ for the mitotic cortex[3]. Furthermore, we estimate the cytoplasmic viscosity η inside the cortical pores to be $\approx 10^{-3}\mathrm{Pa}\cdot\mathrm{s}$ [4]. The length scale t_c is approximated by the previously measured thickness of the cortex ($200\,\mathrm{nm}$) [5]. We thus obtain an estimate of the dissipative (imaginary) term of K_{eff} of the cortex of $\approx 100\,\mathrm{Pa}$ at $f = 10\,\mathrm{Hz}$. This elastic modulus is still more than an order of magnitude lower than the shear modulus of the mitotic cortex at $10\,\mathrm{Hz}$ which can be inferred from[6] to be $\approx 200\,\mathrm{kPa}$. Thus, we expect that the dissipative, imaginary term of K_{eff} gives a small, negligible contribution at frequency $f = 10\,\mathrm{Hz}$ and lower frequencies because $K \gtrsim G$ (provided that $\nu > 0$).

II. INFLUENCE OF INTERNAL VISCOSITY ON CELL MECHANICAL RESPONSE

In the following section, we show that the force response of the liquid interior of a model cell adds $\leq 1\%$ to the effective modulus K of uniaxial compression for cytoplasmic viscosities of up to $1\,\mathrm{Pa}\cdot\mathrm{s}$ and is thus negligible for our study.

In our simulations, we tested the influence of internal cytoplasmic viscosity on the force response of measured cells. To this end, we simulated the time-periodic deformation of model cells, that were constituted by an elastic shell with typical cell parameters and a viscous incompressible (pressurized) interior (Fig. 1). Typical values for the viscosity of the non-cytoskeletal phase of the cytoplasm range between $10^{-3} - 10^{-2}\,\mathrm{Pa}\cdot\mathrm{s}$ [4,7]. From our simulations, we find that the force contribution due to viscous friction generated by cyclic cytoplasmic deformation is negligible up to frequencies of $10\,\mathrm{Hz}$ and viscosities of $1\,\mathrm{Pa}\cdot\mathrm{s}$. There, the calculated effective elastic modulus of the model cell agrees within 1% with the modulus obtained for the case of vanishing internal viscosity (Fig. 1). This finding suggests that cytoplasmic viscosities give a negligible contribution to the mechanical response of cells during our cell-mechanical probing, which is corroborated by earlier experimental findings[6]. At a probing frequency of $10\,\mathrm{Hz}$, we start to see notable changes of the elastic modulus for $\eta = 10\,\mathrm{Pa}\cdot\mathrm{s}$ in simulations (Fig. 1).

III. UNIAXIAL COMPRESSION OF MODEL CELLS AND PHENOMENOLOGICAL LAWS

In the following section, we describe the parametrisation and analysis of model cell compression that were used for generation of the data as presented in the main text, Fig. 2. Finally, we present phenomenological laws that approximate the functional dependencies of effective modulus K and parameter α as found in simulations.

In our study, we performed simulations of a small uniaxial compression step ($\Delta h = 0.5\,\mu\mathrm{m}$) of pressurized elastic shells. Each shell has a thickness of $200\,\mathrm{nm}$, cell volume of $4300\,\mu\mathrm{m}^3$, an area bulk modulus $K_B = 25\,\mathrm{mN/m}$ and an area shear modulus $K_S = 8.3, 10, 15, 20$ or $25\,\mathrm{mN/m}$. For each value of K_S, we simulated compression from an initial reference height of $h_0 = 15, 14, 13, 12, 11$ or $10\,\mu\mathrm{m}$. This was repeated for different values of cortical tension ($\gamma_a = 0.5, 1, 1.5, 2, 2.5$ and $3\,\mathrm{mN/m}$). Therefore, in total $5 \times 6 \times 6 = 180$ simulations have been performed to calibrate the cellular response to uniaxial compression at different mechanical parameters of the cortex. (Furthermore, another 2×180 simulations were performed with equal parameters but deviating bending stiffness testing the influence of changing cortex thickness. There, we assumed i) the absence of bending rigidity or ii) a twofold increased value of

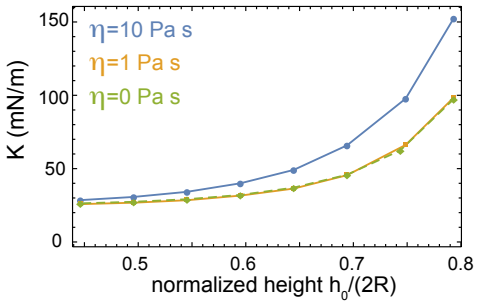

Figure 1. Effective shell moduli calculated from simulations in the presence of a viscous bulk of varying viscosity η. Mechanical parameters of the model cell's shell were $K_B = 25\,\mathrm{mN/m}$, $K_S = 8.33\,\mathrm{mN/m}$, $\gamma_a = 1.5\,\mathrm{mN/m}$, $t = 200\,\mathrm{nm}$. Up to a viscosity of $1\,\mathrm{Pa}\cdot\mathrm{s}$, the influence of the bulk viscosity is negligible. At $\eta = 10\,\mathrm{Pa}\cdot\mathrm{s}$, the bulk viscosity increases the calculated effective modulus of the model cell.

bending rigidity, see Section VI.)
From each simulation, we extracted the force exerted on the elastic shell after compression F_{tot} and calculate the effective elastic modulus of the cortical shell K as described in the main text (see Eqn.(1-4), main text).
We describe the height-dependence of the effective shell elastic modulus as $K(\tilde{h}) \approx K_B(1 + \alpha \exp(\tilde{h}/\lambda))$ (see Eq. 5, main text). In this formula, the coefficient λ was determined from an exponential fit of simulated data by the function $K_B(1+\alpha \exp(\tilde{h}/c))$. We noted, that the fit parameter c varied only slightly in dependence of shell parameters $\tilde{K}_S$ and $\tilde{\gamma}_a$. To spare the characteristic height scale c as a fit parameter for our noisy experimental data, we used henceforth its average value $\lambda = 0.091081$. In turn, we refitted the effective moduli of simulated data by $K_B(1 + \alpha(\tilde{K}_S) \exp(\tilde{h}/\lambda))$ for set values of K_B, K_S and γ_a, providing α as a function of the dimensionless parameters $\tilde{K}_S = K_S/K_B$ and $\tilde{\gamma}_a = \gamma_a/K_B$. For a given value of $\tilde{\gamma}_a$, the dependence of α on $\tilde{K}_S$ is captured by a fit function $C(\tilde{\gamma}_a)\ln[\tilde{K}_S] + D(\tilde{\gamma}_a)$. Finally, the dependence of the fit parameters $C(\tilde{\gamma}_a)$ and $D(\tilde{\gamma}_a)$ on the parameter $\tilde{\gamma}_a$ is captured through a polynomial fit of third degree:

$$C_{fit}(\tilde{\gamma}_a) = (1.09 \cdot 10^{-4} + 1.071 \cdot 10^{-4}\,\tilde{\gamma}_a - 1.54 \cdot 10^{-5}\,\tilde{\gamma}_a^2 + 1.08 \cdot 10^{-6}\,\tilde{\gamma}_a^3),$$
$$D_{fit}(\tilde{\gamma}_a) = (9.418 \cdot 10^{-6} - 5.874 \cdot 10^{-5}\,\tilde{\gamma}_a - 2.157 \cdot 10^{-5}\,\tilde{\gamma}_a^2 + 4.44 \cdot 10^{-6}\,\tilde{\gamma}_a^3).$$

By construction, the resulting function $C_{fit}(\tilde{\gamma}_a)\ln[\tilde{K}_S] + D_{fit}(\tilde{\gamma}_a)$ makes excellent quantitative predictions about the value of α in dependence of $\tilde{\gamma}_a$ and $\tilde{K}_S$ (Fig. 2d, main text).
For simulations with the alternative assumptions of i) twofold bending stiffness and ii) vanishing bending stiffness, we obtain different fit polynomials. For i), we have

$$C_{fit}(\tilde{\gamma}_a) = (1.59 \cdot 10^{-4} + 1.09 \cdot 10^{-4}\,\tilde{\gamma}_a - 1.15 \cdot 10^{-5}\,\tilde{\gamma}_a^2 + 4.4 \cdot 10^{-8}\,\tilde{\gamma}_a^3),$$
$$D_{fit}(\tilde{\gamma}_a) = (-3.09 \cdot 10^{-5} - 5.41 \cdot 10^{-5}\,\tilde{\gamma}_a - 3.68 \cdot 10^{-5}\,\tilde{\gamma}_a^2 + 7.87 \cdot 10^{-6}\,\tilde{\gamma}_a^3).$$

For ii), we find

$$C_{fit}(\tilde{\gamma}_a) = (4.22 \cdot 10^{-5} + 1.5 \cdot 10^{-4}\,\tilde{\gamma}_a - 4.67 \cdot 10^{-5}\,\tilde{\gamma}_a^2 + 6.34 \cdot 10^{-6}\,\tilde{\gamma}_a^3),$$
$$D_{fit}(\tilde{\gamma}_a) = (8.62 \cdot 10^{-5} - 1.65 \cdot 10^{-4}\,\tilde{\gamma}_a + 4.76 \cdot 10^{-5}\,\tilde{\gamma}_a^2 - 8.42 \cdot 10^{-6}\,\tilde{\gamma}_a^3).$$

IV. CELL DEFORMATION SIMULATIONS

Simulations were performed using the finite element (FEM) toolbox AMDiS, developed at the Institute of Scientific Computing TU Dresden[8,9]. We use an axisymmetric Arbitrary Lagrangian Eulerian (ALE) model with incompressible Navier-Stokes equations for the viscous fluid inside the cell, where the two plates and the forces acting on the membrane are implemented as boundary conditions.
We assume the cell to be in a stationary state initially, where elastic parameters have no influence on the force exerted by the cell on the plates. The cell is then compressed by a prescribed sinusoidal decrease of the distance h between the plates, while simultaneously calculating the force exerted on the upper plate.

Using axisymmetry normal to the plates, we can perform calculations on a two dimensional domain describing half of the cell's cross-section. An example image of the simulation domain is shown in Fig. 2. The interior of the cell is denoted by the computational domain Ω which is bounded by the cell cortex/membrane Γ and the symmetry axis. Γ itself is subdivided into the area touching the plates Γ_p and the free surface area Γ_f. During compression a part of the free surface will touch the plate, accordingly Γ_p and Γ_f are time-dependent:

$$\Gamma_p(t) = \{\mathbf{x} = (x_0, x_1) \in \Gamma : x_1 = 0 \vee x_1 = h(t)\}, \qquad \Gamma_f(t) = \Gamma / \Gamma_p(t). \tag{8}$$

The interface curve of Γ for the initial meshes with $h = h_0$ is given by a minimal surface calculated according to equations described in[10].

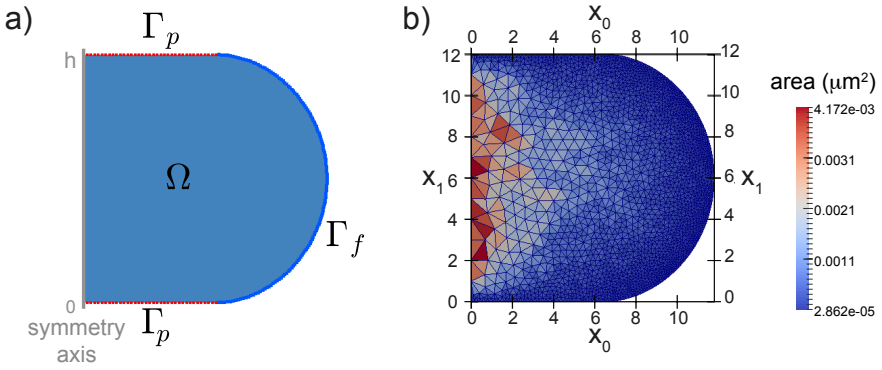

Figure 2. (a) Example image for a simulation domain Ω. The plates here are on the top and bottom sides of the cell with the boundary Γ_p (red dotted line). The free part of the boundary of the cell is Γ_f (blue line). (b) Example image for the mesh for $h_0 = 12\,\mu$m. The color scale indicates the areas of the triangles.

The system is governed by the axisymmetric Navier-Stokes equations[11] together with the surface forces and contact conditions for the plate,

$$\rho\, \partial_t^\bullet \mathbf{v} = \nabla \cdot \mathbf{S} + \frac{\eta}{x_0} \begin{pmatrix} 2\partial_{x_0} v_0 \\ \partial_{x_0} v_1 + \partial_{x_1} v_0 \end{pmatrix} + \frac{2\eta}{(x_0)^2} \begin{pmatrix} v_0 \\ 0 \end{pmatrix}, \qquad \text{in } \Omega \tag{9}$$

$$\nabla \cdot \mathbf{v} + \frac{1}{x_0} v_0 = 0, \qquad \text{in } \Omega \tag{10}$$

$$\mathbf{S} = \eta \left(\nabla \mathbf{v} + \nabla \mathbf{v}^T\right) - p\mathbf{I}, \qquad \text{in } \Omega \tag{11}$$

$$\mathbf{S} \cdot \mathbf{n} = -\frac{\partial E_{\text{tension}}}{\partial \Gamma} - \frac{\partial E_{\text{bend}}}{\partial \Gamma} - \frac{\partial E_{\text{stretch}}}{\partial \Gamma}, \qquad \text{on } \Gamma_f \tag{12}$$

$$[\mathbf{S} \cdot \mathbf{n}]_0 = \left[-\frac{\partial E_{\text{tension}}}{\partial \Gamma} - \frac{\partial E_{\text{bend}}}{\partial \Gamma} - \frac{\partial E_{\text{stretch}}}{\partial \Gamma} \right]_0, \qquad \text{on } \Gamma_p \tag{13}$$

$$v_1 = \delta_{x_1 > 0} \cdot \partial_t h, \qquad \text{on } \Gamma_p \tag{14}$$

$$v_0 = 0, \qquad \text{on } \partial\Omega / \Gamma \tag{15}$$

where ρ is the mass density of cytoplasm, $\partial_t^\bullet \mathbf{v}$ denotes the material derivative of the velocity field $\mathbf{v} = (v_0, v_1)$ of the cytoplasmic fluid, p is the pressure field, η the viscosity, $\mathbf{n}$ the outer unit normal of the domain on Γ, and $\mathbf{S}$ is the bulk stress measured in N/m^2. The first variation of the interfacial energies with respect to changes in Γ yields the interfacial forces. We have[12]

$$\frac{\partial E_{\text{tension}}}{\partial \Gamma} = -2\gamma_a H \mathbf{n}, \quad \frac{\partial E_{\text{bend}}}{\partial \Gamma} = B \left(2\Delta \left(H - H_0\right) + 4\left(2H^2 - K_G\right)\left(H - H_0\right) - 4H\left(H - H_0\right)^2\right) \mathbf{n}, \tag{16}$$

where γ_a is the active surface tension, B is the bending stiffness of the cell cortex, H the mean curvature, H_0 the mean curvature in the initial state, and K_G the gaussian curvature, respectively. Formulas for the calculation of the curvatures of an axisymmetric surface grid can be found in[13].
The formula for the elastic force involves the two principal stretches λ_1 and λ_2, that describe the relative change of the surface length in lateral and rotational direction, respectively:

$$\lambda_1 = \frac{\mathrm{d}s}{\mathrm{d}s_{|t=0}}, \lambda_2 = \frac{x_0}{x_{0|t=0}}, \tag{17}$$

where s is the arc length, x_0 the distance to the symmetry axis, and $s_{|t=0}$ and $x_{0|t=0}$ are the corresponding quantities at the same material point in the initial state. With this, we can write[12]

$$\frac{\partial E_{\text{stretch}}}{\partial \Gamma} = (2H\,\mathbf{n} - \nabla_\Gamma)\left[(K_B + K_S)\,(\lambda_1 - 1) + (K_B - K_S)\,(\lambda_2 - 1)\right] - 2K_S\,(\lambda_1 - \lambda_2)\,\frac{1}{x_0}\begin{pmatrix}1\\0\end{pmatrix}. \tag{18}$$

The discretization is done by an ALE method, where grid points at the cell surface Γ are moved with the velocity $\mathbf{v}$. Interior grid points in Ω are displaced by a harmonic field $\mathbf{w}$ calculated in every time step:

$$\begin{aligned} \Delta \mathbf{w} &= 0, && \text{in } \Omega \\ \mathbf{w} &= \tau \mathbf{v}, && \text{on } \partial\Omega \end{aligned} \tag{19}$$

where τ is the time step size. Whenever a grid point of the free boundary, $\mathbf{x} = (x_0, x_1) \in \Gamma_f$, reaches the lower or upper plate, $x_1 \leq 0$ or $x_1 \geq h$, it is moved exactly onto the plate, i.e. $x_1 = 0$ or $x_1 = h$, respectively, and we mark the point as a member of the discrete points set of Γ_p instead of Γ_f.
The position (and velocity) of the moving plate are prescribed by a cosine function

$$h(t) = h_0 - \frac{\Delta h}{2}\left[1 - \cos\left(2\pi f \cdot (t - t_0)\right)\right], \tag{20}$$

where f is the oscillation frequency. The compression starts at $t = t_0$ and ends at $\tilde{t} = 1/(2f) + t_0$, where maximum compression is reached. For $t > \tilde{t}$, we keep the cell in the compressed state, $h(t) = h_0 - \Delta h$.
The force, exerted on the upper plate, is calculated in every time step using

$$F_{\text{plate}} = 2\pi \int_\Gamma a(x_0, x_1) \cdot x_0 \cdot \left[\mathbf{S} \cdot \mathbf{n}\right]_1 \, \mathrm{d}\Gamma\,. \tag{21}$$

where the factor $2\pi x_0$ emerges due to axisymmetry, a: $\Gamma \to \mathbb{R}$ is the piecewise linear extension of an indicator function for the upper plate:

$$a(x_0, x_1) = \begin{cases} 1 & \text{if} \quad x_1 \geq h \\ 0 & \text{else}\,. \end{cases} \tag{22}$$

After compression, i.e. at height $h_0 - \Delta h$, we have $F_{plate} = F_{tot}$, cf. Eq. (2) main text.
As shown in see Sec. II, we found that the contribution of interior viscosity to the force response is negligible. To simulate the process without interior viscosity, one can take advantage of some simplifications. In this case, we do not need a 2D mesh representing half of the cell's cross section but only a 1D mesh representing the membrane Γ in Fig. 2(a). Accordingly, the Navier-Stokes equations (9)-(13) are replaced by a set of equations that only determine the velocity field on the surface Γ,

$$\mathbf{v} = \mu\left[-\frac{\partial E_{\text{tension}}}{\partial \Gamma} - \frac{\partial E_{\text{bend}}}{\partial \Gamma} - \frac{\partial E_{\text{stretch}}}{\partial \Gamma} - p_c(V - V_0)\,\mathbf{n}\right], \qquad \text{on } \Gamma_f \tag{23}$$

$$\mathbf{v} = \begin{pmatrix} \mu\left[-\frac{\partial E_{\text{tension}}}{\partial \Gamma} - \frac{\partial E_{\text{bend}}}{\partial \Gamma} - \frac{\partial E_{\text{stretch}}}{\partial \Gamma}\right]_0 \\ \delta_{x_1 > 0} \cdot \partial_t h \end{pmatrix}, \qquad \text{on } \Gamma_p \tag{24}$$

where V is the (3D) volume of the cell, V_0 is the volume in the initial state and p_c is a large constant to provide the pressure to ensure volume conservation. In the absence of viscosity, the (inverse) coefficient of friction μ controls the dynamics and must be chosen large enough to keep the system in an equilibrated state. Here we use $\mu = 1.25 \cdot 10^{-7}\,\mathrm{m^2 s/kg}$. We verified numerically that this choice relaxes surface forces from elastic deformation on a time scale much faster than the period of the prescribed height oscillations. In particular μ is large enough that simulation results are invariant to a further increase in μ. Cell volume is conserved by a penalty approach. Being multiplied by the normal vector, the term $p_c(V - V_0)$ plays the role of a pressure. For large p_c this term dominates equation (23) to highest order which leads to $V = V_0$. We have chosen $p_c = 1.2 \cdot 10^5\,\mathrm{N/m^5}$ which is large enough to ensure the relative change in volume is less than 0.01% for all times.
The interfacial forces are implemented explicitly, i.e. curvatures and principal stretches of the configuration in the previous time step are used to calculate the force in the new time step. Therefore, the system is quite restrictive to time step sizes. For the simulations with interior flow, a time step of 0.5μs is used. Hence, for an oscillation frequency of 10Hz we need ≈ 200.000 time steps to simulate a full period of 0.1 s. The initial mesh is shown in Fig. 2(b) for $h_0 = 12\,\mu$m. A fine mesh at the membrane is necessary to produce highly accurate results for the membrane forces. Hence, the triangle sizes amount from approximately $0.003\,\mu\mathrm{m}^2$ at the interface to $0.4\,\mu\mathrm{m}^2$ around the cell center.

V. SCATTER OF ESTIMATED POISSON RATIOS AT DIFFERENT FREQUENCIES

In this section, we present histograms of experimentally measured values $\tilde{K}_S = K_S/K_B$ as well as associated Poisson ratios for all frequencies measured (Fig. 3(a,b)). Furthermore, we discuss fitting of respective distributions and sources of data scatter.
Histograms of $\tilde{K}_S$ are shown in have been fitted with the lognormal distribution of maximum likelihood (Fig. 3(a)). Histograms of Poisson ratio ν are plotted with the distribution induced by the lognormal distribution of $\tilde{K}_S$ (Fig. 3(b)). This induced distribution is calculated by the functional relationship $\nu = (1 - \tilde{K}_S)/(1 + \tilde{K}_S)$.
In Fig. 3(c), we analyzed simulated data in the same way as experimental data, however not using the exact values for cell volume and cell height. Instead, we drew the values of cell volume and cell height from a Gaussian distribution with correct mean value and a standard deviation that matches our error estimate for cell volume and cell height (7.5% and 0.5 μm, respectively). We chose $N = 55$, similar to sample numbers measured in the experiments. The resulting scatter in estimated Poisson ratios is shown in Fig. 3(c), where the horizontal lines indicate median, 25th percentile and 75th percentile. While the median is close to actual values of the Poisson ratio, the resulting scatter is substantial, in particular for $\nu = 0.25$. We conclude that the large scatter of Poisson ratios observed in our experimental data does not exclusively result from mechanical variations between cells but stems to a substantial amount from experimental uncertainties.

VI. INFLUENCE OF CORTICAL THICKNESS AND BENDING STIFFNESS VARIATIONS ON POISSON RATIO ESTIMATES

Cortical thickness in mitotic HeLa cells has previously been estimated to be $\approx 200\,\mathrm{nm}$[5]. However, cells exhibit cell-cell variations in cortical thickness and thus variations in cortical bending stiffness which will contribute to scatter of Poisson ratio estimates in our analysis. In order to examine the influence of cell-cell variations in cortical bending stiffness, we repeated our simulations of cell deformation with i) twofold increased bending stiffness (corresponding to $\approx 40\%$ relative increase in cortex stiffness) and ii) vanishing bending stiffness of the cortical shell. Using these alternative simulations to calibrate cell mechanical response, we reanalyzed our data. Corresponding alternative Poisson ratio estimates are presented in Fig. 4(b) and (c) where results of the original analysis from Fig. 4(c), main text, are depicted again in Fig. 4(a) for direct comparison. We see that i) the assumption of higher bending stiffnesses of the cortex would lead to consistently higher Poisson ratio estimates for cortical shells. Furthermore, we see that ii) assuming vanishing bending stiffness would consistently lead to lower Poisson ratio estimates of cortical shells. In both cases, the change in Poisson ratio estimates is particularly striking for Poisson ratio values substantially below 0.5. In summary, we conclude that i) an underestimation of cortical bending stiffness in our analysis of experimental data would lead to a consistent underestimation of cortical Poisson ratios, while ii) an overestimation of cortical bending stiffness in our analysis would lead to a consistent overestimation of cortical Poisson ratio in particular if cortical Poisson ratio values are substantially below 0.5. Finally, independent of a possible under- or overestimation of absolute values of the Poisson ratio, we find in all cases a significant trend of Poisson ratio increase with decreasing frequency.

VII. THE TWO-DIMENSIONAL POISSON RATIO OF A THIN SHELL

In the following, we show that the two-dimensional Poisson ratio ν_{2D} of a thin shell, made up of a thin layer of an isotropic material, equals the respective three-dimensional Poisson ratio ν of the material.
For the surface energy density of stretching of a thin shell, one obtains in complete analogy to the three-dimensional case[16]

$$F = K_S(\epsilon_{ij} - \frac{\delta_{ij}}{2}\epsilon_{ll})^2 + \frac{1}{2}K_B(\epsilon_{ll})^2, \tag{25}$$

where K_B and K_S are the area bulk modulus and the area shear modulus of the shell and $\epsilon_{ij}, (i, j = 1, 2)$ are in-plane coefficients of the strain tensor. The corresponding stress-strain relationship reads

$$\sigma_{ij} = 2K_S(\epsilon_{ij} - \frac{\delta_{ij}}{2}\epsilon_{ll}) + K_B\delta_{ij}\epsilon_{ll}. \tag{26}$$

Correspondingly, the strain can be written as

$$\epsilon_{ij} = \frac{1}{2K_S}(\sigma_{ij} - \frac{\delta_{ij}}{2}\sigma_{ll}) + \frac{1}{4K_B}\delta_{ij}\sigma_{ll}. \tag{27}$$

We will now determine the expression of the two-dimensional Poisson ratio of a thin shell as a function of K_B and K_S. To this end, we consider the special case of a thin, flat, square-shaped patch of a shell subject to a uniform in-plane stretch through opposite forces acting at the top and bottom edge and with free side edges. Correspondingly, the only non-vanishing stress component is σ_{yy}. According to Eq. 27, the strain tensor is given as

$$\boldsymbol{\epsilon} = \frac{1}{2K_S}\begin{pmatrix} \frac{-\sigma_{yy}}{2} & 0 \\ 0 & \frac{\sigma_{yy}}{2} \end{pmatrix} + \frac{1}{4K_B}\begin{pmatrix} \sigma_{yy} & 0 \\ 0 & \sigma_{yy} \end{pmatrix}. \tag{28}$$

The two-dimensional Poisson ratio ν_{2D} is defined as the ratio $\nu_{2D} = -\epsilon_{xx}/\epsilon_{yy}$. With the above relation (28), this equates to $\nu_{2D} = (K_B - K_S)/(K_B + K_S)$. Using the definitions $K_B = t_c G(1+\nu)/(1-\nu)$ and $K_S = t_c G$ for an isotropic shell material with shear modulus G and Poisson ratio ν, we obtain $\nu_{2D} = \nu$. If the constraint of isotropy is released, the two-dimensional Poisson ratio may adopt values in the range $[-1, 1]$.

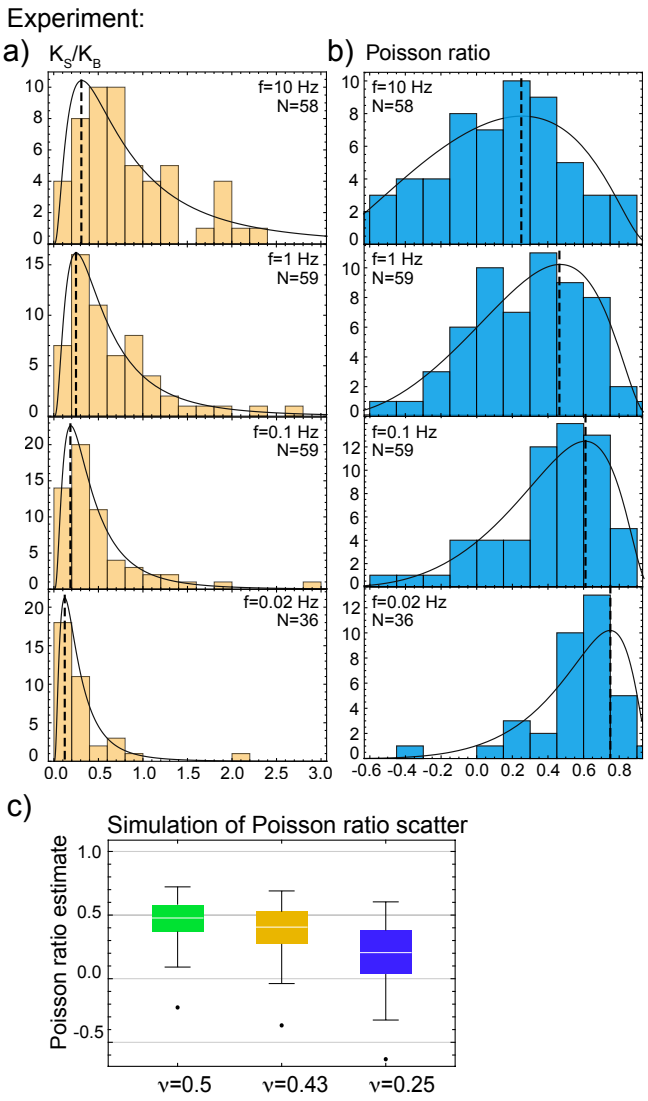

Figure 3. a,b) Results of the analysis of experimental data. a) Histograms of estimated values for the ratio between area shear modulus and area bulk modulus $\tilde{K}_S = K_S/K_B$ with fitted lognormal distributions (logarithmic mean and standard deviation: f=10 Hz, $\mu = -0.31, \sigma = 0.92$; f=1 Hz, $\mu = -0.7, \sigma = 0.82$; f=0.1 Hz, $\mu = -1.03, \sigma = 0.8$; f=0.02 Hz, $\mu = -1.5, \sigma = 0.8$). b) Histograms of estimated Poisson ratios with induced distributions. c) Poisson ratio estimates for simulated data including fake errors of cell volume and cell height. Green data set, $\nu = 0.5$: median: 0.48, IQR: 0.21; orange data set, $\nu = 0.43$: median: 0.41, IQR: 0.25; blue data set, $\nu = 0.25$: median: 0.20, IQR: 0.34, where IQR is the interquartile range, i.e. the distance between 25th and 75th percentile. The sample size was N=55, each, and therefore similar to our experimental sample sizes.

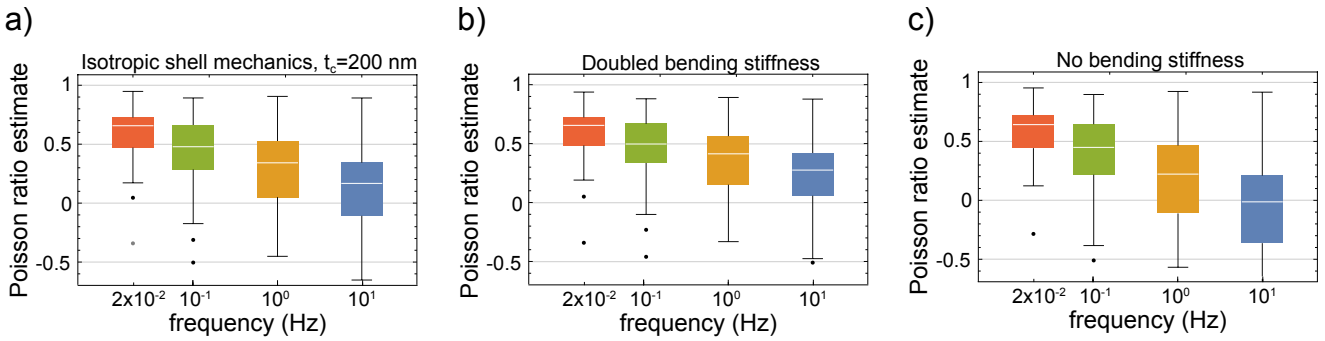

Figure 4. Poisson ratio estimates of the mitotic cortex of HeLa cells using different assumptions on cortical bending stiffness in our analysis (sample sizes from left to right: N=36, N=59, N=59, N=58). a) Estimated Poisson ratios using the assumption of an isotropic cortex with thickness of 200 nm as printed in Fig. 3f, main text. From left to right, median values: 0.66, 0.48, 0.34, 0.17, IQR: 0.26, 0.38, 0.48, 0.45. b) Estimated Poisson ratios using twofold bending stiffness as compared to the analysis in the main text. From left to right, median values: 0.65, 0.5, 0.41, 0.28, IQR: 0.24, 0.33, 0.41, 0.36. c) Estimated Poisson ratios using vanishing bending stiffness. From left to right, median values: 0.64, 0.45, 0.22, -0.013, IQR: 0.3, 0.43, 0.58, 0.57.

REFERENCES

[1]Biot, M. A., and D. G. Willis, 1957. The Theory of Consolidation. 24:594–601.
[2]Granger, R. A., 2012. Fluid Mechanics. Courier Corporation. Google-Books-ID: VWG8AQAAQBAJ.
[3]Charras, G. T., C.-K. Hu, M. Coughlin, and T. J. Mitchison, 2006. Reassembly of contractile actin cortex in cell blebs. 175:477–490.
[4]Kalwarczyk, T., N. Ziębacz, A. Bielejewska, E. Zaboklicka, K. Koynov, J. Szymański, A. Wilk, A. Patkowski, J. Gapiński, H.-J. Butt, and R. Hołyst, 2011. Comparative Analysis of Viscosity of Complex Liquids and Cytoplasm of Mammalian Cells at the Nanoscale. 11:2157–2163.
[5]Clark, A. G., K. Dierkes, and E. K. Paluch, 2013. Monitoring Actin Cortex Thickness in Live Cells. 105:570–580.
[6]Fischer-Friedrich, E., Y. Toyoda, C. J. Cattin, D. J. Müller, A. A. Hyman, and F. Jülicher, 2016. Rheology of the Active Cell Cortex in Mitosis. 111:589–600.
[7]Valentine, M. T., Z. E. Perlman, T. J. Mitchison, and D. A. Weitz, 2005. Mechanical Properties of Xenopus Egg Cytoplasmic Extracts. 88:680–689.
[8]Witkowski, T., S. Ling, S. Praetorius, and A. Voigt, 2015. Software concepts and numerical algorithms for a scalable adaptive parallel finite element method. 41:1145–1177.
[9]Mokbel, M., and S. Aland. An ALE method for simulations of axisymmetric elastic surfaces in flow. .
[10]Fischer-Friedrich, E., A. A. Hyman, F. Jülicher, D. J. Müller, and J. Helenius, 2014. Quantification of surface tension and internal pressure generated by single mitotic cells. 4:6213.
[11]Mokbel, D., H. Abels, and S. Aland, 2018. A phase-field model for fluid-structure interaction. 372:823–840.
[12]Mokbel, M., D. Mokbel, A. Mietke, N. Traber, S. Girardo, O. Otto, J. Guck, and S. Aland, 2017. Numerical simulation of real-time deformability cytometry to extract cell mechanical properties. 3:2962–2973.
[13]Hu, W.-F., Y. Kim, and M.-C. Lai, 2014. An immersed boundary method for simulating the dynamics of three-dimensional axisymmetric vesicles in Navier–Stokes flows. 257:670–686.
[14]Skoufias, D. A., S. DeBonis, Y. Saoudi, L. Lebeau, I. Crevel, R. Cross, R. H. Wade, D. Hackney, and F. Kozielski, 2006. S-Trityl-L-cysteine is a reversible, tight binding inhibitor of the human kinesin Eg5 that specifically blocks mitotic progression. 281:17559–17569.
[15]Stewart, M. P., A. Hodel, A. Spielhofer, C. J. Cattin, D. J. Müller, and J. Helenius, 2013. Wedged AFM-cantilevers for parallel plate cell mechanics. 59:186–194.
[16]Landau, L., and E. Lifshitz, 1986. Theory of Elasticity. Elsevier Ltd., 3rd edition.